RSC Advances

PAPER

View Article Online
View Journal | View Issue

Cite this: *RSC Adv.*, 2017, **7**, 52435

Dual mode temperature sensing through luminescence lifetimes of F- and O-coordinated Cr^{3+} sites in fluorosilicate glass-ceramics†

Changjian Wang,[a] Abhishek Wadhwa,[a] Shuo Cui,[ab] Ronghua Ma,[a] Xvsheng Qiao,* [a] Xianping Fan [a] and Xianghua Zhang[b]

Luminescence lifetime based temperature sensing has an intrinsic immunity to the influence of external conditions, and dual mode thermometry is highly accurate due to its "self-calibration" merit. To develop thermometry with both features, we investigated the phase and microstructural evolution of Cr^{3+}-doped calcium-fluorosilicate glass and glass-ceramics, which revealed different luminescent behavior relating to the different Cr^{3+} sites in the materials. From the photoluminescence (PL) spectra, the emission at 717 nm was derived from the O-coordinated octahedral sites, while the 1 μm super-broad emission was assigned to the F-coordinated octahedral sites. After an annealing treatment, cubic CaF_2 nanocrystals were homogeneously precipitated in the glass-ceramics; thus, both the O-coordination in the residual glass phase and F-coordination in the CaF_2 crystalline phase were strengthened. This led to the enhancement of both the emissions at 717 nm and 1 μm. The O-coordinated sites were relatively strong-field sites in which the fluorescence of Cr^{3+} originated from the radiative transitions of the two thermally coupled energy levels, ^2E and $^4T_2$, while the F-coordinated sites were relatively weak-field sites. Hence, the Cr^{3+} exhibits only one excited state $^4T_2$, which is inactivated by radiative transitions and non-radiative transitions from the thermal quench. Based on the obtained results, the maximum relative temperature sensitivity coefficients are 0.76% K^{-1} at 498 K for the 717 nm emission and 0.47% K^{-1} at 351 K for the 1 μm emission. This provides the possibility of developing a dual mode temperature sensor with high precision only using a single material.

Received 1st October 2017
Accepted 23rd October 2017

DOI: 10.1039/c7ra10864h

rsc.li/rsc-advances

1. Introduction

In recent years, optical temperature sensors have been widely applied in electrical power, chemical, metallurgical and other fields due to their advantages in anti-electromagnetic interference and high sensitivity.[1–3] In order to further improve the accuracy and extend the operating temperature regions of optical temperature sensors, researchers have attempted to utilize multi-active-center doped material systems or new host materials for doping active-center ions.[4–8] These attempts involve a variety of temperature sensing mechanisms, providing ample valuable inspiration for the design of new types of temperature sensors. Among the various types of optical temperature sensors, luminescence-lifetime-based sensors[4] make up a large proportion due to their intrinsic immunity to the influence of external conditions such as those of the excitation beams and optical fiber transmission efficiencies. Trivalent chromium (Cr^{3+}) ions, with the $[Ar]3d^3$ electron configuration, have been widely applied as temperature sensing probes due to their diversity in temperature-dependent lifetimes, which vary with the different host materials used.[9–11] Three equivalent d-electrons in the free Cr^{3+} ion lead to the spectral terms ^4F (ground state), ^4P and ^2G (excited states). In crystals or glasses, the electrostatic interactions between the d-electrons and ligand atoms can modify the spectral terms and induce the splitting of the d-orbital, where ^4F would split into the $^4T_1$ and $^4T_2$ states and ^2G would split into the ^2E, $^2T_1$, $^2T_2$ and $^2A_2$ states. On the basis of crystal field theory,[12,13] the optical properties of Cr^{3+} ions can be manipulated by the coordination of the host lattice or matrix particularly the atoms in the first coordination sphere. This leads to adjustable lowest excited states for the Cr^{3+} ions in various crystal fields. According to the Tanabe–Sugano diagram, ^2E acts as the lowest excited state of Cr^{3+} at a high crystal field strength and is related to a narrow-band red emission (~700 nm) due to the parity and spin doubly forbidden $^2E \rightarrow {}^4A_2$ transition with a long photoluminescence (PL) lifetime. Furthermore, $^4T_2$ would act as the lowest energy state at a low crystal field strength and results in

[a]State Key Laboratory of Silicon Materials, Department of Materials Science and Engineering, Zhejiang University, Hangzhou 310027, China. E-mail: qiaoxus@zju.edu.cn; changjian-wang@zju.edu.cn

[b]UMR-CNRS 6512 "Verres & Ceramiques", Institut de Chimie de Rennes, Universite de Rennes 1, Campus de Beaulieu, 35042 Rennes Cedex, France

† Electronic supplementary information (ESI) available. See DOI: 10.1039/c7ra10864h

a broad-band near-infrared (NIR) emission (~1 μm) due to the parity-forbidden but spin-allowed $^4T_2 \rightarrow {}^4A_2$ transition with a relatively short PL lifetime. Therefore, Cr^{3+} could be a good candidate for dual mode temperature sensing by coordination into different phases with significantly different strength crystal fields in multi-phase materials, such as glass-ceramics.[5,14]

Oxyfluoride glass-ceramics[15–17] have been considered as ideal hosts for various luminescence-active ions due to their high thermal and mechanical stability originating from the oxide glass matrix as well as their excellent spectroscopic merits related to the homogenously precipitated fluoride nanocrystals. Using a convenient heat treatment strategy, the crystal size and crystallinity can be easily controlled. Along with the evolution of both the phase and microstructure, the coordination of Cr^{3+} ions in different sites can be executed. Using this manipulation, one can design the crystal field around the Cr^{3+} ions and then adjust the spectroscopic behavior of the resulting materials.[18]

In this paper, Cr^{3+}-doped oxyfluoride glass-ceramics with homogeneously distributed cubic $CaF_2 : Cr^{3+}$ nanocrystals were prepared upon annealing $50SiO_2$–$20Al_2O_3$–$30CaF_2$ glass. Two significantly different Cr^{3+} sites in the glass-ceramics were identified *via* PL spectroscopy and assigned to the O- and F-coordinated sites with red and NIR emissions, respectively. It follows that the temperature dependent PL lifetimes of Cr^{3+} at the different sites are both suitable for temperature sensing and can be proposed as a dual mode temperature sensing method requiring only the Cr^{3+}-singly-doped glass-ceramics.

2. Experimental procedure

Oxyfluoride glass with the composition $50SiO_2$–$20Al_2O_3$–$29.95CaF_2$–$0.05CrF_3$ (in mol%, named as G) was prepared using a melt-quenching method. The appropriate batch of high purity (3 N) raw materials (silica, alumina, calcium fluoride and chromium fluoride) was placed in a covered corundum crucible and melted at 1500 °C for 45 min in air. Plain glasses were obtained by quenching the melt between two brass plates. Then, the subsequent crystallization temperatures (580 °C, 600 °C, 620 °C and 640 °C) were selected between the glass transition temperature (T_g) and the first crystallization temperature (T_{x1}) (Fig. S1†). The glass-ceramics GC580, GC600, GC620 and GC640, named after their annealing temperature, were obtained by annealing the glass at the abovementioned temperatures for 2 h in the air.

Differential thermal analysis (DTA) measurements were carried out on a CDR-1 differential thermal analyzer with a fixed specimen weight of 60 mg. X-ray diffraction (XRD) measurements were performed on a DIMAX-RA X-ray diffractometer (Rigaku Corporation, Tokyo, Japan) using Cu-K_α radiation at a scan rate of 2° min^{-1}. Transmission electron microscopy (TEM) and high resolution transmission electron microscopy (HRTEM) measurements were conducted to check the fine crystal structure using a CM200 (Philips, Eindhoven, the Netherlands) microscope. Photoluminescence (PL) spectra, including the excitation spectra, emission spectra and temperature dependent luminescence decay curves, were collected using a FLSP920 spectrometer (Edinburgh Instrument Ltd., Livingston, UK) equipped with a TAP-02 temperature controller.

3. Results and discussion

3.1 Phase and microstructure

The glass-ceramics have a typical two-phase structure, where the cubic CaF_2 lattice grew up to the nanoscale in the glass matrix and Cr^{3+} enlarged the lattice as an interstitial dopant. As shown in the XRD patterns (Fig. 1(a)), the as-quenched glass (sample G) exhibits a typical amorphous feature without any sharp diffraction peaks. In contrast, the glass-ceramics show sharp XRD peaks and the diffraction intensity became stronger upon increasing the annealing temperature, indicating the precipitation of FCC (face centered cubic) structured CaF_2 (JCPDS # 35-0816). Calculated using the Scherrer equation, the average crystal size could be estimated to be about 10, 13, 15 and 20 nm for GC580, GC600, GC620 and GC640, respectively. Moreover, the higher annealing temperatures also led to a higher crystallinity of CaF_2 in the glass-ceramics. Furthermore, the diffraction peaks of the FCC CaF_2 crystals in the investigated glass-ceramics shifted to lower diffraction angles (2θ) as compared to those of the standard JCPDS card (# 35-0816). For GC620, the calculated lattice parameter of the precipitated nanocrystals was 5.490 Å, which was higher than the standard value (5.463 Å). This was clear evidence of crystal lattice expansion, indicating the enrichment of Cr^{3+} ions into the CaF_2 lattice. It was unlikely that the Cr^{3+} (0.62 Å) would substitute Ca^{2+} (1.2 Å) due to the related lattice shrinkage effect. From the data obtained for the Ca^{2+} radius (1.2 Å in octahedral

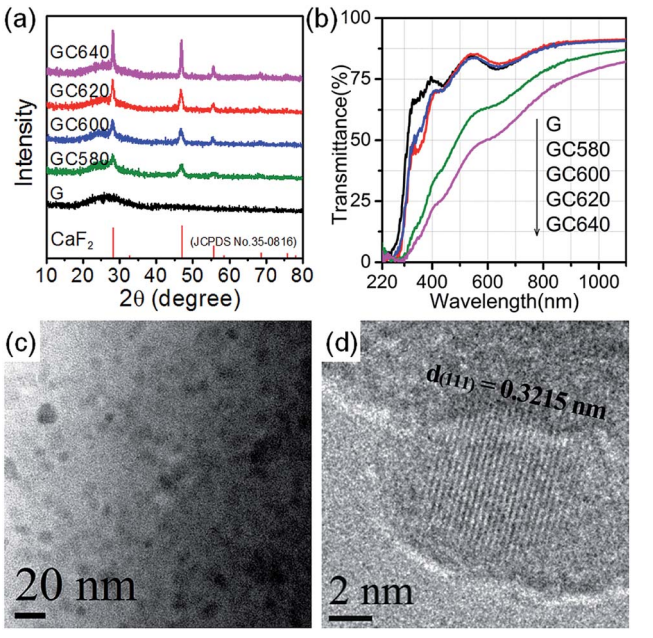

Fig. 1 X-ray diffraction patterns (a) and transmittance spectra (b) of the Cr^{3+}-doped glass and glass ceramics fabricated using different annealing procedures. The TEM (c) and HRTEM (d) images of the Cr^{3+}-doped glass-ceramics obtained after annealing at 600 °C for 2 h (GC600).

coordination) and F^- radius (1.23 Å in tetrahedral coordination), the largest radii of the ions occupying the tetrahedral and octahedral interstices in cubic CaF_2 were calculated to be 0.27 Å and 0.50 Å, respectively. Hence, Cr^{3+} ions exhibit a higher probability to occupy the octahedral interstice and enlarge the octahedron. In addition, the glass and the glass-ceramics obtained upon annealing at temperatures lower than 600 °C (GC580 and GC600) maintain high transparency in the visible-light spectral region (Fig. 1(b)). However, in annealing at temperatures higher than 620 °C (GC620 and GC640), the glass-ceramics apparently lose their transparency. This was due to the large crystal size and crystallinity of the precipitated CaF_2 in GC620 and GC640 (Table 1). In the transmittance spectra, two visible absorption bands were assigned to the $^4A_2 \rightarrow {}^4T_1$ (centered at 440 nm) and $^4A_2 \rightarrow {}^4T_2$ (centered at 640 nm) energy level transitions of the Cr^{3+} ions Fig. 1(b).

The transmission electron microscopy (TEM, Fig. 1(c)) and high-resolution TEM (HRTEM, Fig. 1(d)) images display the precipitated CaF_2 nanocrystals in GC600 with crystal sizes of ~10–15 nm, which are dispersed homogeneously in the glass host. This is consistent with the crystal size calculated from the XRD patterns using the Scherrer equation. The CaF_2 nanocrystals in the HRTEM image exhibited a well-defined lattice structure, and the interplanar spacing was calculated to be 0.3215 nm using a fast Fourier transform (FFT) algorithm. The interplanar spacing corresponds to the (111) plane of cubic CaF_2 (0.3155 nm, JCPDS # 35-0816). Similar to the XRD results, the calculated interplanar spacing (d = 0.3215 nm in Fig. 1(d)) was larger than the standard value. This indicates that a number of Cr^{3+} ions have entered the precipitated CaF_2 crystalline phase, occupied the octahedral interstice, and enlarged the interplanar spacing.

3.2 Photoluminescence (PL)

The PL emission spectra (Fig. 2(a) and (c)) of the glass and glass-ceramics show different broad emission bands centered at 717 nm and 1 μm when excited at 296 nm and 464 nm, respectively. Here, the sharp zero-phonon lines (R-lines at ~700 nm), observed due to the $^2E \rightarrow {}^4A_2$ transition, could not be found in the spectra (Fig. 2(a)), which could be because the glass matrix inhomogenously broadened the zero-phonon lines.[19] Thus, the emission may be assigned to ^2E, $^2T_1 \rightarrow {}^4A_2$, while the 1 μm emission may be attributed to $^4T_2 \rightarrow {}^4A_2$. It was believed that these two clearly distinguishable emissions were related to the different Cr^{3+} sites coordinated with O^{2-} (717 nm) and F^- (1 μm) in the glass and glass-ceramics, respectively.[20] This will be further discussed in Section 3.3. By monitoring the emission at 717 nm, three broad excitation bands were recorded centered at

Table 1 The crystal size and crystallinity of the Cr^{3+} ion doped glass-ceramics

	GC580	GC600	GC620	GC640
Crystal size (nm)	10.4 ± 1.1	13.4 ± 1.0	15.5 ± 1.1	20.5 ± 1.3
Crystallinity (%)	17.0 ± 0.5	24.8 ± 0.5	31.6 ± 0.5	35.6 ± 0.6

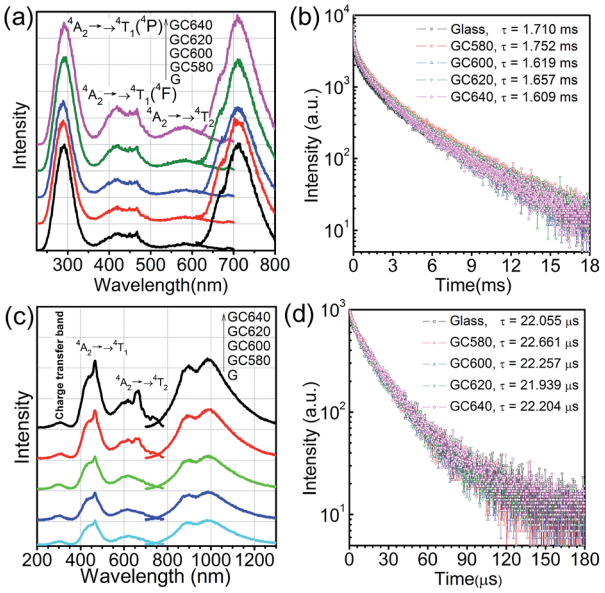

Fig. 2 The PL emission and excitation spectra (a, c) as well as the PL decay curves (b, d) of the Cr^{3+}-doped glass-ceramics fabricated using the different annealing procedures: (a and b) by exciting at 296 nm and monitoring at 717 nm; (c and d) by exciting at 464 nm and monitoring at 1 μm.

296 nm, 419 nm and 586 nm, corresponding to charge transfer band, Cr^{3+}: $^4A_2 \rightarrow {}^4T_1$ transition and Cr^{3+}: $^4A_2 \rightarrow {}^4T_2$ transition, respectively. By monitoring at 1 μm, the three excitation bands corresponding to charge transfer band, Cr^{3+}: $^4A_2 \rightarrow {}^4T_1$ transition and Cr^{3+}: $^4A_2 \rightarrow {}^4T_2$ transition still exist. However, all three bands were red-shifted to longer wavelengths and located at 306 nm, 438 nm and 617 nm. As the annealing temperature was increased, the 717 nm emission was improved very limitedly; however, the 1 μm emission intensity showed a significant enhancement. This could be due to the enhancement of the O^{2-} or F^- coordination of Cr^{3+} during the growth of the new phase (CaF_2 nanocrystals).

The PL decay curves were recorded by monitoring the emission at 717 nm or 1 μm, as shown in Fig. 2(b) and (d). The PL decay curves were best fitted to double-exponential functions, which could be described by the following equation:

$$I(t) = A_1 \exp\left(-\frac{t}{\tau_1}\right) + A_2 \exp\left(-\frac{t}{\tau_2}\right), \quad (1)$$

where τ_1 and τ_2 are the long- and short-decay components respectively, and parameters A_1 and A_2 are fitting constants. According to eqn (1), the average lifetime $\langle\tau\rangle$ is given by:

$$\langle\tau\rangle = \frac{A_1\tau_1^2 + A_2\tau_2^2}{A_1\tau_1 + A_2\tau_2}. \quad (2)$$

According to eqn (2), the average lifetimes of the 717 nm and 1 μm luminescence were evaluated to be stable at about 1.6–1.7 ms and 22–23 μs, respectively. The average lifetime of 717 nm was much longer than that of 1 μm, which was consistent with assigning the 717 nm emission to the ^2E, $^4T_2$

→ $^4A_2$ transition (partiy- and spin-forbidden for ^2E) and assigning the 1 μm emission to the $^4T_2 \rightarrow {}^4A_2$ transition (parity-forbidden but spin-allowed).

3.3 O^{2-}- or F^- coordination

Fluorosilicate glass probably constitutes both silicate and fluoride glassy matrices.[21] Hence, the glass and glass-ceramics could provide F- and O-coordinated sites for Cr^{3+}. On one hand, the silicate matrix is a random network of [SiO_4] tetrahedra, to which modifiers such as CaO were added to break up the networks and stabilizers such as Al_2O_3 were added to prevent crystallization.[19] Breakage of the Si–O covalent bonds by the modifiers produce approximately octahedral arrangements of O^{2-}. The Cr^{3+} ions prefer to occupy these octahedral sites rather than the tetrahedral sites. On the other hand, the fluoride matrix formed by the [AlF_6] octahedral and polyhedral [CaF_8] also exist in the fluorosilicate glass host, where the Cr^{3+} ions can easily substitute Al^{3+} to occupy the octahedral sites. Alkaline earth fluorides such as CaF_2 act as modifiers in the fluoride matrix and are easily crystallized from the matrix. According to the phase and microstructural analysis (Fig. 1), the Cr^{3+} ions also enter the precipitated CaF_2 crystalline phase of the glass ceramics, occupying the octahedral interstice and enlarging the interplanar spacing. As a result, the Cr^{3+} ions were octahedrally coordinated with O^{2-} and F^-, and displayed two different luminescence behaviors. Upon increasing the annealing temperature, the crystallinity of the precipitated CaF_2 gradually increases, so that more Cr^{3+} ions are surrounded by the CaF_2 lattice and subsequently, the 1 μm emission was enhanced (Fig. 2(c)). The F/O ratio of the residual glassy phase was reduced to a lower level due to the crystallization of CaF_2 and thus, the O^{2-} coordination environment was significantly enhanced. However, such an O^{2-} coordination enhancement was too small to significantly influence the PL intensity (Fig. 2(a)).

The energy level structure of Cr^{3+} is highly dependent on the crystal field strength and determines the different PL behaviour of the O-coordinated and F-coordinated Cr^{3+} ions. The energy level structures of transition metal ions are usually determined by the relative strengths of the octahedral crystal ligand field splitting parameter, D_q, and the Racah parameters, B and C. Solutions to the multi-electron crystal-field Hamiltonian are represented on Tanabe–Sugano diagrams,[22,23] in which the normalized multiplet energies, $E(\Gamma)/B$, are plotted as a function of D_q/B, for a constant value of C/B, where Γ denotes the irreducible representation of the electronic state. In inorganic glass or crystals, the Cr^{3+}ions prefer to occupy the sites exhibiting a nearly perfect octahedral symmetry because of the strong ligand field stabilization energy of Cr^{3+} in a six-fold coordination geometry.[24] As illustrated in the Tanabe–Sugano diagram (Fig. 3(a)), in an octahedral crystal field the ^4F of Cr^{3+} will split into $^4A_2$, $^4T_2$ and $^4T_1$, while ^2G would split into ^2E, $^2T_1$, $^2T_2$ and $^2A_1$. The $^4A_2$ state has the lowest energy and serves as the ground state. The energy difference between ^2E and $^2T_1$ or $^2T_2$ and $^4A_2$ was almost constant or varies slightly in all the fields; however, the energy difference between $^4T_2$ and $^4A_2$ varies significantly

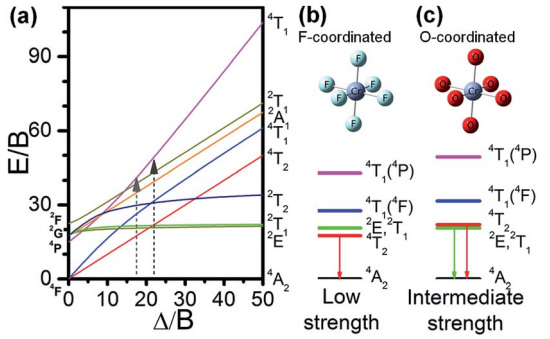

Fig. 3 Tanabe–Sugano diagram of Cr^{3+} ions in the octahedral crystal field (a); energy levels of the Cr^{3+} ions coordinated with F^- (b) in a low crystal field strength and with O^{2-} in an intermediate crystal field strength (c).

upon changing the crystal field. The studies of both Tanabe[25,26] and Casalboni[27] clearly show the relationship between the energy of the different excited states of Cr^{3+} ions and D_q/B. In weak crystal-field sites, where $D_q/B < 2.3$, the lowest excited state was an orbital triplet $^4T_2$, from which broadband PL is observed due to the enhancement of the phonon assisted $^4T_2 \rightarrow {}^4A_2$ transitions. For strong crystal fields ($D_q/B > 2.3$), the lowest excited state was changed to ^2E and the spectrum consists of narrow zero-phonon lines (R lines) with vibrationally induced sidebands due to the $^4T_2 \rightarrow {}^4A_2$ transitions. For intermediate crystal fields ($D_q/B \approx 2.3$), mixing between $^4T_2$ and ^2E occurs and the observed photoluminescence spectrum, even at low temperature, is a superposition of the broad $^4T_2 \rightarrow {}^4A_2$ band on the $^2E \rightarrow {}^4A_2$ R line and its phonon sideband.

The strength D_q of the octahedral crystal field and the Racah parameter B can be determined from the peak energies of the $^4A_2 \rightarrow {}^4T_2$ and the $^4A_2 \rightarrow {}^4T_1$ transitions.[28] In octahedral symmetry, the energy difference between the $^4A_2$ and $^4T_2$ states is equal to $10D_q$, which is measured from the peak energy (ν_1) of the $^4A_2 \rightarrow {}^4T_2$ absorption band:

$$D_q = \frac{\nu_1}{10}. \quad (3)$$

The value of B is determined from the energy value (ν_1) of $^4A_2 \rightarrow {}^4T_2$ and the energy value (ν_2) of $^4A_2 \rightarrow {}^4T_1$, is given by

$$B = \frac{(2\nu_1 - \nu_2)(\nu_2 - \nu_1)}{3(9\nu_1 - 5\nu_2)}. \quad (4)$$

According to the absorption spectra (Fig. 1(b)), the glass and the glass-ceramics have almost the same average values for ν_1 and ν_2, and thus have the same values of $D_q = 1571.3\ cm^{-1}$, $B = 734.1\ cm^{-1}$ and $D_q/B = 2.14$.

As a matter of fact, the PL spectra (Fig. 2) revealed two types of Cr^{3+} sites: the O^{2-} octahedrally coordinated sites (centered at 717 nm) and the F^- octahedrally coordinated sites (centered at 1 μm) in the glass and glass-ceramics. Herein, in order to evaluate the crystal field strengths of the [CrO_6] and [CrF_6] octahedra, the PL excitation peak wavelengths were used to deduce the values of ν_1 and ν_2; then, the D_q/B values were evaluated as 2.5 and 2.3

for $[CrO_6]$ and $[CrF_6]$, respectively. Thus, the energy level diagrams of the F^- octahedrally coordinated (Fig. 3(b)) and O^{2-} octahedrally coordinated (Fig. 3(c)) sites were elicited from the Tanabe–Sugano diagram (Fig. 3(a)). O^{2-} coordination has an intermediate crystal field with first excited states of ^2E and $^2T_1$, while F^- coordination has a weak crystal field with a lower first excited state, $^4T_2$. This was consistent with the increasing trends of D_q/B correlated with the anion packing densities along the following sequence: fluoride → silicate → borate. Silicate glasses provide relatively strong-field sites, while fluoride and fluorozirconate glasses provide weak-field sites only and the luminescence observed is only a broad $^4T_2 \rightarrow {}^4A_2$ band with a large Stokes red-shift.[19,20,28] Accordingly, when compared with O-coordinated Cr^{3+} (717 nm), the PL emission of F-coordinated Cr^{3+} ions show a red-shift to 1 μm and shorter PL lifetimes. Such a situation was also clearly observed with the excitation bands. When monitored at 1 μm, the three broad excitation bands show red-shifts to longer wavelengths when compared with those monitored at 717 nm. In addition, the charge transfer band monitored by the 1 μm emission was much weaker than those monitored by the 717 nm emission. This can be deduced from the larger electron density related to O^{2-} compared to F^-.

3.4 Temperature sensing performance

To explore the possible applications of dual-model temperature-dependent decay lifetimes in optic temperature sensors, the PL decay curves for the Cr^{3+}-doped GC640 sample from room temperature to about 300 °C (Fig. 4(a) and (b)) were recorded by monitoring at 717 nm and 1 μm. The evaluated lifetimes for both Cr^{3+} sites appear to decrease with temperature (Fig. 4(c) and (d)). Such temperature dependent relationships are mainly due to the thermally activated repopulation between the ^2E and $^4T_2$ states. The $^2E \rightarrow {}^4A_2$ transition is doubly forbidden by parity

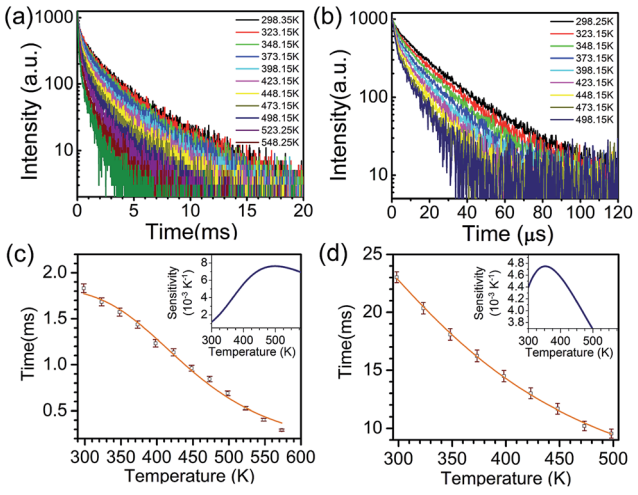

Fig. 4 The 296 nm excited 717 nm luminescence decay curves (a) and the 464 nm excited 1 μm luminescence decay curves (b) obtained for GC640 at different temperature. The fitted relationships of the luminescence lifetimes of Cr^{3+} and temperature (c and d), where the insets show the sensitivity at the investigated temperature ranges.

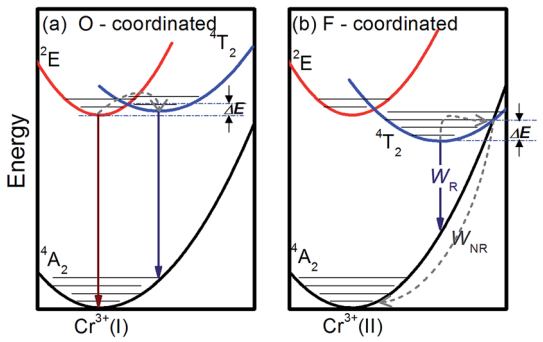

Fig. 5 Simplified energy level diagrams of Cr^{3+} at the different sites in the investigated glass-ceramics: (a) O-coordinated sites and (b) F-coordinated sites.

and spin, which has a longer decay time than the $^4T_2 \rightarrow {}^4A_2$ transition (spin-allowed).

For O-coordinated sites, the ^2E, $^2T_1$, $^4T_2$ and $^4A_2$ energy states were proposed as interrelated, as Fig. 5(a) illustrates, in a configuration coordinate model, where ^2E serves as the lowest excited state and easily intersects with the upper state, $^4T_2$, by the assistance of only a few phonons. Upon increasing the temperature, more electrons repopulate from ^2E to $^4T_2$, resulting in short PL decay lifetimes.[9] Theoretically, the total number of excited ions can be expressed as: $n = n_E + n_T$, where n_E and n_T represent the number of ions at ^2E and $^4T_2$,respectively. The particles at the two levels follow the Boltzmann distribution: $\frac{n_E}{n_T} = C\ \exp(-\Delta E/k_B T)$, where C is the degeneration ratio of ^2E to $^4T_2$, with a value of 3. The decay rate of the total excited state ions is represented by the following expression: $\frac{dn}{dt} = -\frac{1}{\tau}n = -\frac{1}{\tau_E}n_E - \frac{1}{\tau_T}n_T$. Therefore, by solving the equation: $-\frac{1}{\tau}n = -\frac{1}{\tau_E}n_E - \frac{1}{\tau_T}n_T$, the lifetime was obtained as:

$$\tau = \tau_E \frac{1 + 3\ \exp(-\Delta E/k_B T)}{\frac{\tau_E}{\tau_T} + 3\ \exp(-\Delta E/k_B T)}. \quad (5)$$

The sensitivity could be calculated using the following equation:

$$S = \left|\frac{1}{\tau}\frac{d\tau}{dT}\right| = 3\ \exp(-\Delta E/k_B T)\frac{\Delta E}{k_B T^2} \times \left(\frac{1}{1 + 3\ \exp(-\Delta E/k_B T)} - \frac{\tau_E}{\tau_T + \tau_E\ \exp(-\Delta E/k_B T)}\right). \quad (6)$$

Thereby, the PL lifetime data of 717 nm from 298.35 K to 573.25 K were well fitted as the solid line using the least-square method, as shown in Fig. 4(c). The correlation coefficient (R^2) reached 0.99. The parameters τ_E, τ_T and ΔE were determined to be 1.835 ms, 0.008 ms and 2044.5 cm^{-1}, respectively. In addition, the sensitivity curve reaches a maximum of 0.76% K^{-1} at 498 K, as shown in the inset of the Fig. 4(c).

For the F-coordinated sites, the ^2E, $^2T_1$, $^4T_2$ and $^4A_2$ energy states were proposed as interrelated using a configuration

Table 2 The optical thermometry performance of some Cr^{3+} ion-doped materials

Materials	ΔE (cm^{-1})	T_{max} (K)	S_{max} (% K^{-1})	Ref.
$Y_3Al_5O_{12} : Cr^{3+}$	—	—	0.50	31
$LiAl_5O_8 : Cr^{3+}$	—	447	0.83	32
Ruby ($Al_2O_3 : Cr^{3+}$)	1637	390	0.48	33
$LiSrAlF_6 : Cr^{3+}$	4557	333	1.80	34
$Ga_2O_3 : Cr^{3+}$ (in glass-ceramics)	1215	386	0.59	5
O-coordinated Cr^{3+} (in glass-ceramics)	2044	498	0.76	This work
F-coordinated Cr^{3+} (in glass-ceramics)	898	351	0.47	This work

coordinate model as illustrated in Fig. 5(a), where $^4T_2$ serves as the lowest excited state. The large Stokes shift and weak crystal field at the F-coordinated sites enhance the decay rate of (W_{NR}) from the $^4T_2$ excited state to the $^4A_2$ ground state. It thus becomes a predominant factor to significantly reduce the 1 μm PL lifetime as shown in Fig. 4(b). Theoretically, the Mott–Seitz model was used to describe this mechanism quantitatively.[29] The total transition probabilities of the $^4T_2$ state are comprised of radiative (W_R) and non-radiative (W_{NR}) transition probabilities:

$$\frac{1}{\tau(T)} = \frac{1}{\tau_R} + \frac{1}{\tau_{NR}}, \quad (7)$$

where τ_R is the radiative lifetime and τ_{NR} is the non-radiative lifetime. As illustrated in Fig. 5(b), an electron in the $^4T_2$ state would cross the barrier ΔE to the ground state by absorbing a certain amount of phonons.[30] We assumed that τ_R was independent of temperature, while τ_{NR} is dependent of temperature; the relationship between τ_{NR} and temperature can be expressed using the Arrhenius equation:

$$\frac{1}{\tau_{NR}} = \frac{1}{\tau_{NR(0)}}\exp(-\Delta E/k_B T), \quad (8)$$

where $\tau_{NR(0)}$ is the non-radiative decay time at 0 K, ΔE is the energy barrier mentioned above and k_B is the Boltzmann constant. Accordingly, when the temperature increases, the non-radiative decay will become stronger. Through the deformation of the formulae (7) and (8), the total (experimentally measured) lifetime can be written as:

$$\tau(T) = \frac{\tau_R}{1 + \frac{\tau_R}{\tau_{NR(0)}}\exp(-\Delta E/k_B T)}, \quad (9)$$

Then, the sensitivity was calculated using the following equation:

$$S = \left|\frac{1}{\tau}\frac{d\tau}{dT}\right| = \frac{\tau_R}{\tau_R + \tau_{NR(0)}\exp(\Delta E/k_B T)}\frac{\Delta E}{k_B T^2}. \quad (10)$$

We used this equation to fit the lifetime data of the 1 μm emission observed for the GC640 sample. The solid line shown in Fig. 4(d) was the least-squares curve fitting to the lifetime data from 298.25 K to 498.15 K. Impressively, the correlation coefficient (R^2) reached as high as 0.999. This not only expounded the temperature-dependence of the lifetime in the experimental temperature range but also guaranteed the effectiveness of the temperature sensing. Through the fitting, the corresponding parameters τ_R, τ_{NR} and ΔE were determined to be 32.814 μs, 0.997 μs and 898.3 cm^{-1}, respectively. In addition, the sensitivity curve reaches a maximum of 0.47% K^{-1} at 351 K as shown in the inset of the Fig. 4(c).

Based on the abovementioned temperature sensing parameters, comparable performances could be expected for optical thermometries upon introducing the Cr^{3+}-doped fluorosilicate glass-ceramic materials. As a comparison, the temperature sensing parameters of some typical materials reported in the literature are listed in Table 2. The O-coordinated Cr^{3+} in the glass-ceramics exhibit maximum sensitivity ($S_{max} = 0.76\%\ K^{-1}$), which was slightly lower than that observed for $LiAl_5O_8 : Cr^{3+}$, but still better than those reported for $Y_3Al_5O_{12} : Cr^{3+}$, $Al_2O_3 : Cr^{3+}$ (ruby) and $Ga_2O_3 : Cr^{3+}$ in glass-ceramics and with a higher work temperature ($T_{max} = 498$ K). The F-coordinated Cr^{3+} in the glass-ceramics showed the maximum sensitivity ($S_{max} = 0.47\%\ K^{-1}$) at $T_{max} = 351$ K, which was similar to that observed in $Al_2O_3 : Cr^{3+}$ (ruby), so it could also be a good candidate material for optical thermometry. When compared with crystalline and ceramic materials, the glass-ceramics have the further advantages of good designability, easy molding, cost-efficient and so on. Therefore, these types of Cr^{3+}-doped glass-ceramics are very promising candidates for developing a type of dual mode optical thermometry.

4. Conclusion

In fluorosilicate glass-ceramics comprising homogenous cubic CaF_2 nanocrystals, Cr^{3+}ions occupied two different types of sites: one was the O-coordinated octahedral sites in the residual glass phase and the other was the F-coordinated octahedral sites were distributed not only in the residual glass phase but also in the nanocrystalline CaF_2 phase. A certain number of Cr^{3+}ions entered the precipitated CaF_2 nanocrystals, occupying the octahedral interstice and induced an expansion of the fluorite cube lattices. The 717 nm emission was derived from the O-coordinated octahedral sites, while the 1 μm super-broad emission was assigned to the F-coordinated octahedral sites. Upon annealing, the crystal size and crystallinity of the CaF_2 nanocrystals could be enlarged, thus the F-coordinated octahedral Cr^{3+} sites were enhanced and the PL at 1 μm became stronger.

The O-coordinated sites were relatively strong crystal field sites, so the 717 nm emission originates from the radiative transitions of the two thermally coupled ^2E and $^4T_2$ energy levels of Cr^{3+}. In contrast, the F-coordinated sites were relatively weak-field sites, thus $^4T_2$ alternatively served as the lowest excited state and a low vibrational level of $^4T_2$ was easily tunneled to a high vibrational level of the ground state as a result of a thermal quench in non-radiative transition. Accordingly, the temperature dependent PL lifetimes could be theoretically described by eqn (5) and (9). By mean square fitting methods, the maximum relative temperature sensitivity coefficients were 0.76% K^{-1} at 498 K for the 717 nm PL lifetime and 0.47% K^{-1} at 573 K for the 1 μm PL lifetime. These results are comparable with some other typical optical temperature sensing materials, providing evidence of the potential to apply glass-ceramics in highly sensitive, dual mode, self-calibrated PL-lifetime-based temperature sensing.

Conflicts of interest

There are no conflicts to declare.

Acknowledgements

This work was supported by the National Natural Science Foundation of China (No. 51672243), the Program for International S&T Cooperation Projects of China (No. 2014DFB50100), Zhejiang Provincial Natural Science Foundation of China (No. LY16E020003) and the Fundamental Research Funds for the Central Universities (No. 2016QNA4005; No. 2016FZA4007). The authors are very grateful to the support of their research team and for involving one of the authors (Shuo Cui) in the sample preparation and spectral measurements. Associate Prof. Xvsheng Qiao gave a detailed and patient guidance to this work.

References

1 X. Wang, Q. Liu, Y. Bu, C. S. Liu, T. Liu and X. Yan, *RSC Adv.*, 2015, **105**, 86219–86236.
2 X. D. Wang, O. S. Wolfbeis and R. J. Meier, *Chem. Soc. Rev.*, 2013, **42**, 7834–7869.
3 A. H. Khalid and K. Kontis, *Sensors*, 2008, **8**, 5673–5744.
4 M. D. Chambers and D. R. Clarke, *Annu. Rev. Mater. Res.*, 2009, **39**, 325–359.
5 D. Chen, Z. Wan and Y. Zhou, *Opt. Lett.*, 2015, **40**, 3607–3610.
6 A. K. Singh, P. Shahi, S. B. Rai and B. Ullrich, *RSC Adv.*, 2015, **21**, 16067–16073.
7 H. Lu, H. Hao, G. Shi, Y. Gao, R. Wang, Y. Song, Y. Wang and X. Zhang, *RSC Adv.*, 2016, **60**, 55307–55311.
8 S. Liu, S. Liu, M. Zhou, X. Ye, D. Hou and W. You, *RSC Adv.*, 2017, **59**, 36935–36948.
9 Z. Zhang, K. T. V. Grattan and A. W. Palmer, *Phys. Rev. B*, 1993, **48**, 7772–7778.
10 Y. L. Hu, Z. Y. Zhang, K. T. V. Grattan, A. W. Palmer and B. T. Meggitt, *Sens. Actuators, A*, 1997, **63**, 85–90.
11 Y. R. Shen and K. L. Bray, *Phys. Rev. B*, 1997, **56**, 10882–10891.
12 H.-H. Schmidtke and J. Degen, in *Stereochemistry and Bonding*, Springer, 1989, pp. 99–124.
13 A. Luci, T. Castrignano, U. Grassano, M. Casalboni and A. Kaminskii, *Phys. Rev. B*, 1995, **51**, 1490.
14 D. Chen, Z. Wan, Y. Zhou, X. Zhou, Y. Yu, J. Zhong, M. Ding and Z. Ji, *ACS Appl. Mater. Interfaces*, 2015, **7**, 19484–19493.
15 M. J. Dejneka, *J. Non-Cryst. Solids*, 1998, **239**, 149–155.
16 Y. Wang and J. Ohwaki, *Appl. Phys. Lett.*, 1993, **63**, 3268–3270.
17 C. Liu and J. Heo, *J. Am. Ceram. Soc.*, 2012, **95**, 2100–2102.
18 P. I. Macfarlane, K. Holliday, J. Nicholls and B. Henderson, *J. Phys.: Condens. Matter*, 1995, **7**, 9643.
19 B. Henderson, M. Yamaga, Y. Gao and K. O'Donnell, *Phys. Rev. B*, 1992, **46**, 652.
20 F. Rasheed, K. O'Donnell, B. Henderson and D. Hollis, *J. Phys.: Condens. Matter*, 1991, **3**, 3825.
21 J. Zhao, R. Ma, X. Chen, B. Kang, X. Qiao, J. Du, X. Fan, U. Ross, C. Roiland and A. Lotnyk, *J. Phys. Chem. C*, 2016, **120**, 17726–17732.
22 S. Sugano, *Multiplets of transition-metal ions in crystals*, Elsevier, 2012.
23 B. Henderson and G. F. Imbusch, *Optical spectroscopy of inorganic solids*, Oxford University Press, 2006.
24 J. Fernández, M. Illarramendi, R. Balda, M. Arriandiaga, J. Lucas and J. Adam, *J. Non-Cryst. Solids*, 1991, **131**, 1230–1234.
25 Y. Tanabe and S. Sugano, *J. Phys. Soc. Jpn.*, 1954, **9**, 753–766.
26 Y. Tanabe and S. Sugano, *J. Phys. Soc. Jpn.*, 1954, **9**, 766–779.
27 M. Casalboni, V. Ciafardone, G. Giuli, B. Izzi, E. Paris and P. Prosposito, *J. Phys.: Condens. Matter*, 1996, **8**, 9059.
28 F. Rasheed, K. O'Donnell, B. Henderson and D. Hallis, *J. Phys.: Condens. Matter*, 1991, **3**, 1915.
29 L. Bøtter-Jensen, S. W. McKeever and A. G. Wintle, *Optically stimulated luminescence dosimetry*, Elsevier, 2003.
30 M. Ren, C. D. Brites, S.-S. Bao, R. A. Ferreira, L.-M. Zheng and L. D. Carlos, *J. Mater. Chem. C*, 2015, **3**, 8480–8484.
31 H. Aizawa, T. Katsumata, Y. Kiyokawa, T. Nishikawa, T. Sasagawa, S. Komuro, T. Morikawa, H. Ishizawa and E. Toba, *Measurement*, 2006, **39**, 147–152.
32 X. Li, G. Jiang, S. Zhou, X. Wei, Y. Chen, C. K. Duan and M. Yin, *Sens. Actuators, B*, 2014, **202**, 1065–1069.
33 H. Seat and J. Sharp, *IEEE Trans. Instrum. Meas.*, 2004, **53**, 140–154.
34 Z. Zhang, K. Grattan and A. Palmer, *Optical Fiber Sensors Conference*, IEEE Xplore, 1992, pp. 93–96.